Engineering Structures 46 (2013) 332–349

Contents lists available at SciVerse ScienceDirect

Engineering Structures

journal homepage: www.elsevier.com/locate/engstruct

Numerical simulation for steel brace members incorporating a fatigue model

Suhaib Salawdeh, Jamie Goggins *

College of Engineering & Informatics, National University of Ireland, Galway, Ireland

ARTICLE INFO

Article history:
Received 28 September 2011
Revised 20 July 2012
Accepted 30 July 2012
Available online 13 September 2012

Keywords:
Bracing
Cold-formed structural steel
Concentrically braced frames
Earthquake engineering
Fatigue
Numerical modelling

ABSTRACT

The aim of this paper is to develop a robust numerical model for cold-formed steel square and rectangular structural hollow sections for use as axial loaded members in earthquake engineering applications. Pseudo-static cyclic physical tests of cold-formed steel brace specimens using axially loading are used to develop and calibrate a robust numerical model that mimics the results from the tests. A nonlinear fibre based beam-column element model which considers the spread of plasticity along the element is used. This numerical model includes a low cyclic fatigue model, which wraps the nonlinear fibre based beam-column element material in order to capture fracture in the braces. New parameters to be used for the fatigue model are introduced in this paper. Comparisons of the maximum tensile force (F_{max}), initial buckling load (F_c), number of cycles to fracture, the total energy dissipated (W_{tot}) and the energy dissipated at the first cycle of ductility of 4 ($W_{\mu=4}$) between the numerical models and the physical tests are carried out. In general, the models captured the salient response parameters observed in the physical tests. It is found that the numerical model gives a good prediction of the maximum measured tensile force (F_{max}) and initial buckling load (F_c) with the mean values being 0.93 and 0.95 of those measured in the physical tests, respectively. The corresponding coefficients of variation (C_V) are 0.11 and 0.08, respectively. Moreover, the mean values of the total energy dissipated (W_{tot}) and the energy dissipated at the first cycle of ductility of 4 (W_{μ}=4) for the numerical model are found to be 1.12 and 0.98, of those measured in the physical tests, respectively. The corresponding coefficients of variation (C_V) are 0.13 and 0.20, respectively. Furthermore, the numerical model was validated using another set of independent physical tests. This validated brace element model can be used in future numerical models of concentrically brace frames buildings to predict the performance of the complete structures under earthquake loading.

1. Introduction

The brace element is the main element in concentrically braced frame (CBF) systems that undergoes inelastic deformations to dissipate energy during seismic actions. It is destined to carry reversal axial forces in which it may experience yield in tension, buckle in compression or may fracture due to the demand cycles it is expected to endure during seismic actions. Structural hollow sections (square, rectangular, circular and oval shaped) are commonly used as braced elements. Furthermore, increased interest has been shown in studying the performance of hollow structural steel sections [1–19] in order to model their inelastic behaviour.

In this paper, the hysteretic behaviours of cold-formed square and rectangular hollow steel sections (SHS and RHS) subjected to inelastic cyclic loading carried out by Goggins [20] are studied. A robust numerical model for cold-formed carbon steel square and rectangular structural hollow sections is developed. The model is then validated by comparing its predictions to findings by Nip et al. [19] for cold-formed carbon steel hollow sections. Its applicability to cold-formed stainless steel and hot rolled carbon steel square and rectangular structural hollow sections is also investigated. The numerical model could then be employed in non-linear time history analysis (NLTHA) modelling to assess the behaviour of CBF systems.

2. Cyclic tests of steel brace specimens

Goggins [20] carried out many cyclic tests on cold-formed square and rectangular hollow steel sections in order to obtain experimental data to validate numerical models. In particular, the performance of fifteen specimens fabricated from 20×20×2.0SHS, 40×40×2.5SHS and 50×25×2.5RHS sections with normalised slenderness ratios, λ, defined in Eurocode 3 [21], of between 0.4 and 3.2 subjected to cyclic tests were investigated. Two different lengths of specimens (1100 and 3300mm) were used to obtain the broad range of slenderness ratios. The tests carried out by Goggins [20] on intermediate and long length brace specimens were subjected

* Corresponding author. Tel.: +353 91492609; fax: +353 91494507.
E-mail addresses: Suhaib.Salawdeh@nuigalway.ie (S. Salawdeh), Jamie.Goggins@nuigalway.ie (J. Goggins).

0141-0296/$ - see front matter © 2012 Elsevier Ltd. All rights reserved.
http://dx.doi.org/10.1016/j.engstruct.2012.07.036

Notations

A_g	the gross cross sectional area
BRB	buckling restrained brace
CBFs	concentrically braced frames
CF	cold-formed
CS	carbon steel
DI	damage from cyclic loading
DI_i	damage for each amplitude of cycling
e_y	axial yield displacement
E	Young's modulus
f_y	yield strength
f_{ya}	the increased average yield strength due to cold working
f_{yb}	the basic yield value of sheet taken from coupon tests
f_u	the basic ultimate tensile strength of sheet taken from coupon test
F_c	initial buckling load
F_{max}	the maximum tensile force
HR	hot-rolled
HSS	hollow structural section
k	numerical coefficient that depends on the type of forming
m	Fatigue ductility exponent
n	the number of 90° bends in the cross-section
n	current number of cycles
n	number of integration points per element
n_i	Number of cycles at an amplitude
N_f	fatigue life
N_{fi}	Number of constant amplitude cycles of that amplitude necessary to cause failure
NLTHA	non-linear time history analysis
r	radius
RHS	Rectangular hollow sections
S_a	stress amplitude
SHS	square hollow sections
SS	stainless steel
t	the design core thickness of the steel material before cold forming
W_{tot}	total energy dissipated
$W_{\mu=4}$	energy dissipated at the first cycle of ductility of 4
$\Delta\varepsilon_p$	Plastic strain amplitude
ε_o	Fatigue ductility coefficient
λ	Normalised slenderness ratio
μ_f	ductility at fracture

to increasing amplitude cyclic displacements. For these cyclic tests, the loading was applied according to the provisions of the ECCS [22]. The recommended complete testing procedure was followed, for which the axial deformation history is shown in Fig. 1. This implies using one cycle at each level of 0.25, 0.5, 0.75 and 1.0e_y, followed by three cycles at each level of 2, 4, 6e_y, etc., where e_y represents the estimated axial yield displacement. Yield displacements evaluated from the monotonic tensile tests on short specimens were used to determine the amplitudes of the cycles [16].

Nip et al. [19] carried out 16 cyclic tests on square and rectangular hollow steel section in order to study the cyclic response of tubular bracing members of three structural materials: hot-rolled carbon steel, cold-formed carbon steel and cold-formed stainless steel. These specimens were fabricated from 40×40×3.0SHS, 40×40×4.0SHS, 50×50×3.0SHS, 60×60×3.0SHS and 60×40×3.0RHS sections with normalised slenderness ratios between 0.34 and 1.4. They were subjected to increasing amplitude cyclic displacements, similar to the loading regime used by Goggins [20]. Three different lengths of specimens (1250mm, 2050mm and 2850mm) were used. In this paper, the physical tests carried out by Goggins [20] are used to calibrate a numerical model that can capture fracture of the specimens. The numerical model will then be validated by comparing its performance to the results from the physical tests by Nip et al. [19].

Throughout this paper test ID's are identified by member size (depth X width X thickness X length), material (either carbon steel, CS, or stainless steel, SS), forming process (either hot-rolled, HR, or cold-formed, CF); tests carried out by Goggins [20] are followed by the letter G with the specimen number and tests carried out by Nip et al. [19] are followed by the letter N with the specimen number. Test ID's are given in Tables 1 and 2, together with normalised slenderness ratios of the brace about the minor axis (λ_{y-y}) and the measured yield stress of the sections (f_y).

In order to study the behaviour of concentrically braced members, a brief discussion of the hysteretic response (axial load-axial displacement response) of the brace 40×40×2.5×1100-CS-CF-G1 tested by Goggins [20] is presented here. Fig. 2 shows the 40×40×2.5×1100-CS-CF-G1 bracing test specimen with the results from the test showing the hysteretic behaviour of the

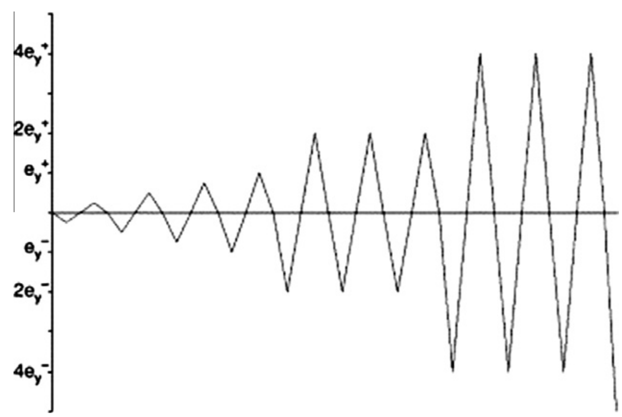

Fig. 1. Cyclic displacement waveform for ECCS procedure.

specimen, which is described by the hysteretic response of axial force plotted against resulting axial displacements [20]. Compression loads are negative and tension loads are positive. The area under the hysteretic curves represents the hysteretic energy dissipated by the brace.

As shown in the hysteretic response in Fig. 2b, the loading was applied according to the provisions of the ECCS [22] discussed earlier. After the occurrence of the first buckling in compression at Point 1, for stockier members the compressive strength decreased as a plastic hinge formed at the mid-height of the brace and next to the connection with the stiffener. For slender members, the member experienced mainly elastic buckling. For all members, their compressive resistance degraded significantly in subsequent cycles of the same axial deformation demand primarily due to residual deformations from previous cycles, and to a lesser extent due to the Baushinger effect (an increase in tensile yield strength causes decrease of the compressive yield strength), similar conclusions were found by Goggins [20] and Tremblay [9]. At every cycle, the brace accumulated permanent elongation. The amount of inelastic rotation imposed to the hinge at every cycle increased as the brace elongated and the imposed deformation increased [9,20]. As the

Table 1
Parameters and results for the specimens used to calibrate the numerical model.

Specimen ID	$\lambda_{y\text{-}y}$	f_y (MPa)	Initial camber (%)	No. of cycles to fracture		Numerical model/ physical tests			
				Physical tests	Numerical model	F_{max}	F_c	W_{tot}	$W_{\mu=4}$
40×40×2.5×1100-CS-CF-G1[a]	0.40	285	0.10	16	14	1.06	0.99	1.15	1.13
40×40×2.5×1100-CS-CF-G2[a]	0.40	285	0.10	15	14	1.07	1.02	1.19	1.12
20×20×2.0×1100-CS-CF-G3[a]	0.90	304	0.50	26	16	0.99	0.87	0.72	1.16
20×20×2.0×1100-CS-CF-G4[a]	0.90	304	0.50	17	16	0.98	1.03	1.31	1.14
50×25×2.5×1100-CS-CF-G5[a]	0.60	304	0.30	16	14	1.05	0.90	1.06	1.22
50×25×2.5×1100-CS-CF-G6[a]	0.60	304	0.30	16	14	1.04	1.00	1.27	1.18
40×40×2.5×3300-CS-CF-G7[b]	1.30	344	0.50	–	–	0.91	1.03	1.07	0.88
40×40×2.5×3300-CS-CF-G8[b]	1.30	350	0.50	–	–	0.93	1.02	1.09	0.89
40×40×2.5×3300-CS-CF-G9[b]	1.30	332	0.50	–	–	0.89	0.99	1.06	0.78
20×20×2.0×3300-CS-CF-G10[a]	3.20	443	1.00	7	4	0.81	0.82	–	–
20×20×2.0×3300-CS-CF-G11[a]	3.00	399	1.00	7	4	0.79	0.79	–	–
20×20×2.0×3300-CS-CF-G12[a]	3.00	399	1.00	7	4	0.76	0.92	–	–
50×25×2.5×3300-CS-CF-G13[b]	1.90	312	1.00	–	–	1.00	1.00	1.22	0.85
50×25×2.5×3300-CS-CF-G14[b]	2.20	428	1.00	–	–	0.85	1.00	1.16	0.74
50×25×2.5×3300-CS-CF-G15[b]	2.20	428	1.00	-	-	0.84	0.92	1.14	0.70
Mean						0.93	0.95	1.12	0.98
C_V						0.11	0.08	0.13	0.20

[a] Tested to failure.
[b] Tested to maximum displacement ductility demand of between 5.6 and 9.5 without specimen failure.

Table 2
Parameters and results for the specimens used to validate the numerical model.

Specimen ID	$\lambda_{y\text{-}y}$	f_y (MPa)	Initial camber (%)	No. of cycles to fracture		Numerical model/ physical tests			
				Physical tests	Numerical model	F_{max}	F_c	W_{tot}	$W_{\mu=4}$
60×60×3.0×2050-CS-HR-N16[a]	0.57	458	0.20	10	11	1.14	1.14	1.67	1.25
40×40×3.0×2050-CS-HR-N17[a]	0.89	478	0.50	19	14	1.01	1.19	0.80	1.25
40×40×3.0×1250-CS-HR-N18[a]	0.50	478	0.20	14	9	1.01	1.05	0.89	1.40
60×60×3.0×2050-CS-CF-N19[a]	0.53	361	0.20	10	11	0.88	0.92	1.92	1.49
40×40×4.0×2050-CS-CF-N20[a,c]	0.89	410	0.50	13	15	0.95	1.00	1.89	1.27
40×40×3.0×2050-CS-CF-N21[a,c]	0.90	451	0.50	10	13	0.98	0.98	2.30	1.28
40×40×3.0×1250-CS-CF-N22[a]	0.50	451	0.20	10	9	0.97	1.01	1.05	1.24
60×60×3.0×2850-SS-CF-N23[a]	0.89	483	0.50	9	13	1.17	0.92	2.63	1.18
50×50×3.0×2850-SS-CF-N24[a]	1.16	552	0.50	13	14	1.03	1.00	1.45	1.13
60×40×3.0×2850-SS-CF-N25[a,c]	1.40	538	0.50	10	16	1.17	0.85	2.74	1.14
60×60×3.0×2050-SS-CF-N26[a]	0.62	483	0.30	10	10	1.15	1.00	1.38	1.20
50×50×3.0×2050-SS-CF-N27[a]	0.80	552	0.50	10	10	1.18	0.93	1.44	1.21
60×40×3.0×2050-SS-CF-N28[a]	0.97	538	0.50	10	12	1.18	0.95	1.96	1.19
Mean						1.08	1.00	1.62	1.25
C_v						0.09	0.09	0.36	0.07

[a] Tested to failure.
[c] Failed at end condition during physical test.

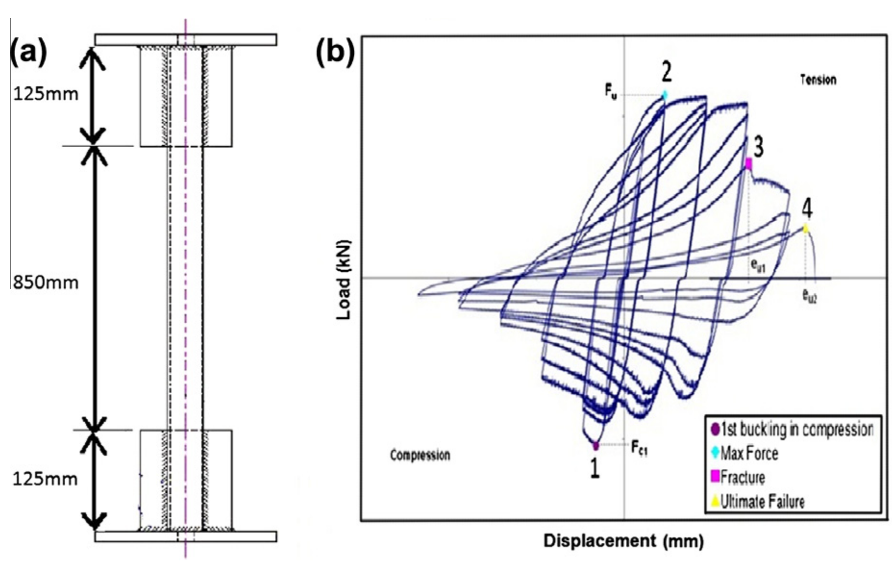

Fig. 2. (a) Specimen diagram and (b) experimental load–displacement response of the specimen 40×40×.2.5×1100-CS-CF-G1 [20].

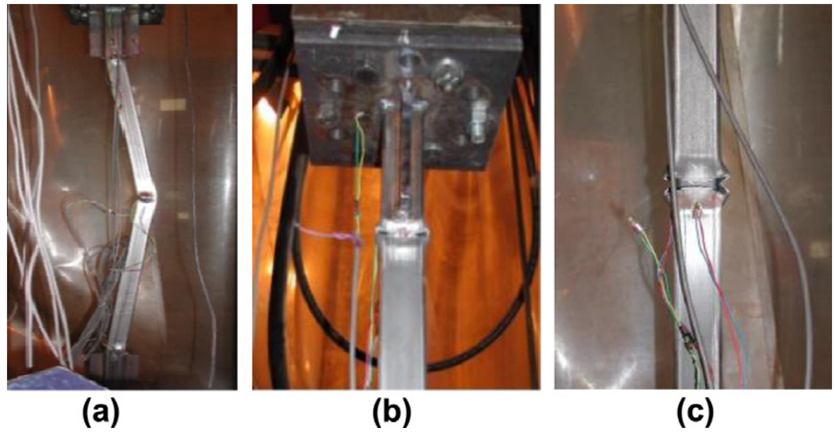

Fig. 3. Failure of specimen 40×40×2.5×1100-CS-CF-G1. (a) Lateral and local buckling. (b) Fracture across local buckled area near top stiffener. (c) Fracture across local buckled are at mid-height of the specimen [20].

brace is stocky with slenderness ratio, λ, of 0.4, local buckling of the cross section developed at the hinge location at mid-height and close to the end stiffeners, which induced high localised strains in the steel material and contributed to reduce the brace compressive strength further. Maximum tension force obtained is shown at Point 2. Fracture took place at the hinges at Point 3 when the brace was stretched in tension after local buckling has occurred, and the ultimate failure occurred at Point 4. The described failure of the specimen above is shown in Fig. 3. It should be noted that the above sequence of behaviour was observed for the stockier members only (e.g. those specimens with normalised slenderness less than 1.3). For more slender specimens (e.g. those specimens with normalised slenderness greater than 1.3), little or no local buckling was observed during the tests. However, premature fracture occurred for specimens with high slenderness ratios (i.e. specimens with slenderness ratio of 3.2). Eurocode 8 [23] specifies limits to the normalised slenderness ratio between 1.3 and 2.0 for concentrically braced frames with X diagonal bracing and suggests to use low width to thickness ratio and Class 1 cross-section defined in Eurocode 3 [21]. Further details on specimens and physical test set-up as well as specimen performance in low cyclic fatigue loading are given in [16].

3. Numerical modelling of steel brace elements

The computational framework Open System for Earthquake Engineering Simulation (OpenSees) [24] is used in this study to develop numerical models of structural steel hollow section brace elements that capture the salient features of the response of these elements to low-cycle tension-compression loading. OpenSees uses the physical-theory models to represent the braces. Two ways to represent the physical theory models are found in Opensees. The first is distributed plasticity, which considers the spread of plasticity along the element and is used for this paper. The second is concentrated plasticity (also known as lumped plasticity), where the interior of the element behaves elastically with plasticity considered to be concentrated over specified hinge lengths at the element ends.

The main limitation in the physical theory model used in OpenSees is that plane sections are assumed to remain plane and it does not account for the section distortion and the local buckling, so the accuracy of the model is degraded after the occurrence of the local buckling. This limitation can be ignored by calibrating the parameters of the numerical model to represent test models.

A numerical model to be used in OpenSees for brace members was proposed by Uriz [25], which is able to model the effect of global buckling. Uriz [25] also calibrated a material model that can be incorporated in the numerical model to account for the effects of low cyclic fatigue, which will be discussed and implemented in Section 4.

Many parameters affect the behaviour of the numerical brace model, such as initial camber, number of integration points and number of elements. These will be studied in the following paragraphs in order to obtain a robust numerical model that can be validated using the data from physical member tests. A graph of the numerical model setup is shown in Fig. 4. This model matches the general characteristic of the physical test specimens, including the specimen length, end conditions and material properties for each individual cyclic test specimen used. End stiffeners were also modelled. Fixed end conditions were provided except for the axial displacement at the loaded end (Point 5 at Fig. 4). The numerical model will first be developed using fifteen cyclic tests carried out by Goggins [20] and then be validated using sixteen cyclic tests carried out by Nip et al. [19].

The uniaxial Giuffre–Menegotto–Pinto steel material model with isotropic strain hardening and the monotonic envelop shown in Fig. 5 is used in this study. However, a low value of strain hardening (<0.008) was used in this study. A nonlinear fibre beam–column element model based on the force formulation proposed by Spacone et al. [26] is employed. This model considers the spread of plasticity along the element through integration of material response over the cross section and subsequent integration of section response along the element. The inelastic beam-column element is derived by small deformation theory, which is used for computation of local stresses and strains along the element. In accordance to the corotational theory described by Filippou and Fenves [27], nonlinear geometry under large displacements is accounted for during transformation of the element forces and deformations to the global reference system. By using the corotational theory the moderate to large deformation effects of inelastic buckling of the concentric brace can be presented (small strains and large displacements). Using this approach, the brace needs to be subdivided into at least two inelastic beam-column elements. However, it is may be necessary to divide the brace into more elements to represent accurately local deformations and steel strains at the critical sections.

In order to get accurate buckling loads and hysteretic behaviour, Opensees represents elements by fibres. Uriz [25] noted that when there are fewer fibres representing the cross section, sensitivity to the interaction between moment and axial loads increased and a

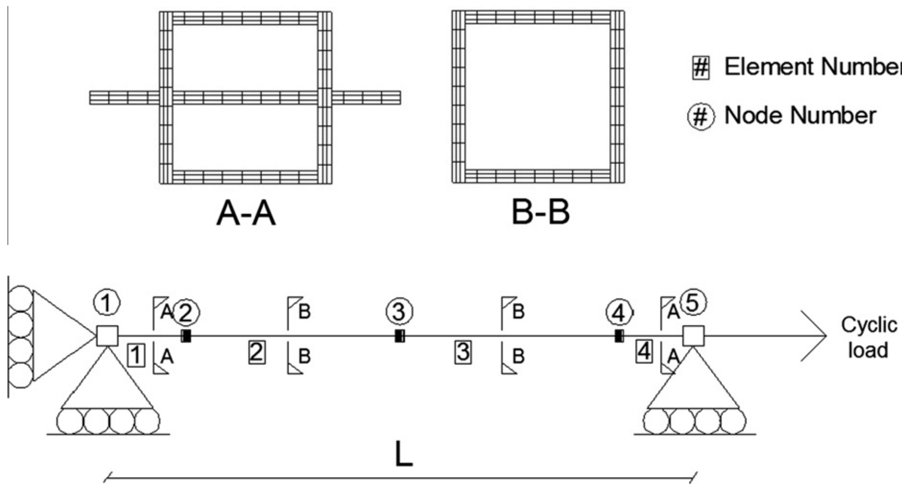

Fig. 4. Setup and loading direction of the numerical model used in OpenSees.

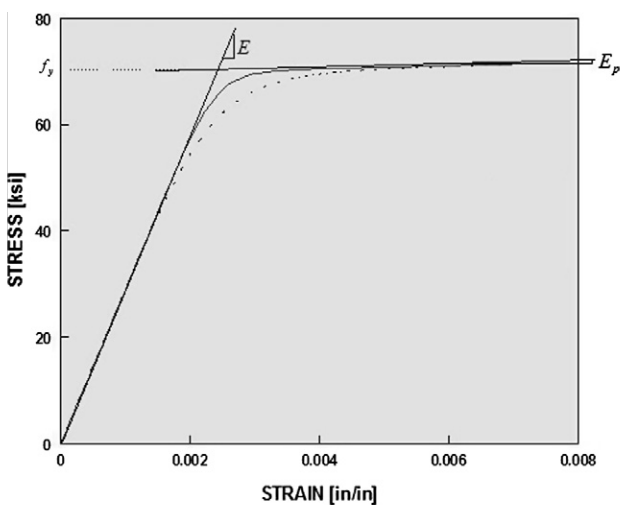

Fig. 5. Monotonic envelop for uniaxial Giuffre-Menegotto-Pinto steel material [24].

loss of stiffness is found when Opensees numerically integrates to determine the area moment of inertia. When there are fewer fibres representing the same area, lower centroid for the fibres will be achieved and the equivalent moment of inertia will be smaller than the cross section with more fibres. This calculation is more sensitive to the number of fibres across the thickness than the number of fibres around the perimeter. For the numerical model used in this paper, it was found that employing three fibres across the thickness and a minimum of $2(b + h)/3$ fibres around the perimeter of the cross section was optimum in terms of computational effort and accuracy, where b and h are the width and the height of the cross section in mm. Thus, in total a minimum of 180 fibres are used in the cross section.

In OpenSees, in order to consider buckling in an axially loaded brace, it is essential to include an imperfection either to the geometry of the brace in the form of initial camber or to the properties of the member in the form of a residual stress distribution over the cross section. In this model, initial camber is used to consider buckling. Uriz [25] proposed to use an initial camber displacement at mid-length of the brace with a magnitude varied between 0.05% and 0.1% of the brace length, whereas Wijesundara [28] recommends to use the initial camber displacement at mid-length of 0.5% of the brace length.

By using small initial cambers between 0.05% and 0.1% the buckling is delayed to reach and the buckling force is overestimated as shown in Fig. 6. On the other hand, incorporating initial cambers of 0.5% was not representing the observed response of many braces. For this study, initial camber between 0.1% and 1.0% is found to give satisfactory results, where the lower bound is used for stockier specimens and larger initial camber values are used for more slender specimens, as will be shown in Section 5. It is also noted that for a brace member with specified material and section properties, the initial camber is the main parameter that plays the major role for determining the first buckling load in the numerical model, but does not affect the general behaviour of the hysteretic response.

Fig. 7 shows the effect of changing the number of non-linear beam column elements for the unstiffened length of the brace in the numerical model for the force displacement response using three integration points per element and constant initial camber of 0.5% of the length of the brace. By changing the number of non-linear beam column elements, the first buckling strength is nearly identical and relatively insensitive to the number of sub-elements but depends upon initial camber value used. However, the brace modelled with two elements resists less force than a brace modelled with four elements in the post buckling range with a maximum difference of 18.7% (Fig. 7). Similarly, a brace modelled with eight elements resists slightly less force in the post buckling range than the brace modelled with four elements with a maximum difference of 5.8% (Fig. 7). The brace modelled with sixteen elements has nearly identical behaviour in the post buckling range and the internal curvature with the brace modelled with eight elements. However, there was a maximum difference of 1% in the post buckling range at the second loop, but it was nearly identical for other loops. As expected, the internal curvature and the post buckling range are more accurately represented when more elements are used with three integration points per element. From the above, it is noted that a minimum number of elements of eight should be used while using three integration points. On the other hand, it is expected that less elements can be used in the brace when more integration points are assigned, in order to minimise the time needed for modelling and computational efforts.

The integration along the element is based on Gauss–Lobatto quadrature (integration) rule (two integration points at the element ends) [24]. This numerical quadrature rule interpolates polynomial displacements of order $2n - 3$ exactly, where n is the number of integration points. However, due to nonlinear material properties, these polynomial interpolants may not be physically

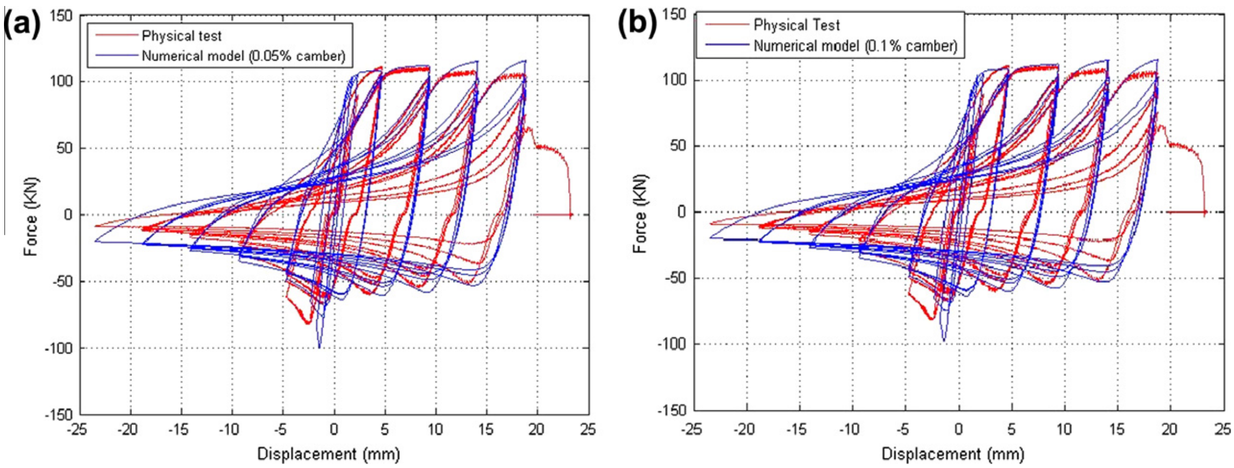

Fig. 6. Experimental force–displacement response of specimen 50×25×2.5×1100-CS-CF-G5 compared to the hysteretic model found from OpenSees with (a) 0.05% initial camber and (b) 0.1% initial camber.

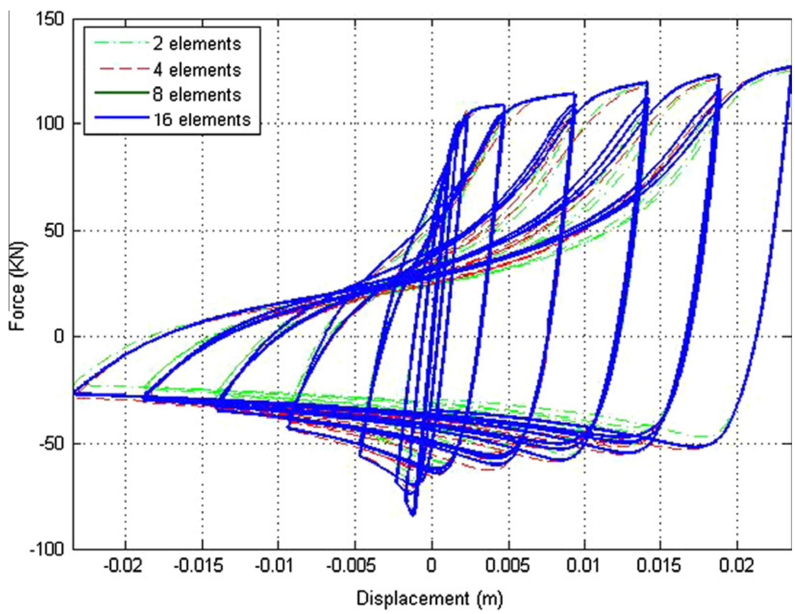

Fig. 7. Effect of changing the number of non-linear beam column elements to represent the unstiffened length for the brace in the numerical model to the force displacement response using three integration points per element.

accurate, which may result in distributions of deformations that are not adequately described by polynomials [25]. Uriz [25] observed that the specimen with only two integration points exhibits a slightly more dramatic loss of compressive strength in the post-bucking range. This can also be seen in Fig. 8. This is due to an under integration of the element. Under-integration of element response is not recommended and the minimum number of integration points recommended for every inelastic beam–column element is 3 [25]. In Fig. 8, the brace was divided into eight elements and different integration points were used for every element. While using two integration points, slightly lower compression resistance in the post buckling range is observed as compared to models containing three, five and seven integration points with a maximum difference of 18%. However, nearly identical results in hysteretic response were found in models containing three, five, and seven integration points, as observed in Fig. 8

To check the interaction between the number of elements of the brace and the number of integration points per element, a comparison of the response of the numerical models was conducted by changing the number of elements and the number of integration points per element as follows: eight elements with three integration points per element, six elements with four integration points per element, four elements with six integration points per element and two elements with ten integration points per element, which is the maximum integration points that can be used for an element in OpenSees. Fig. 9 shows that when a finer subdivision is used by dividing the brace into a number of elements or dividing the sub-element into number of integration points the results are nearly identical. Thus, two elements with 10 integration points per element for the buckling brace could be a suitable choice.

A sensitivity analysis on the predicted behaviour of the model containing two elements and various numbers of integration points (3, 4, 5, 6, 8 and 10) was conducted (see Fig. 10). It is concluded that two elements and three integration points cannot accurately represent the real hysteretic response of brace members. There is a slight difference in the behaviour when using four and five integration points. However, nearly identical results were found when using six, eight and ten integration points. In this

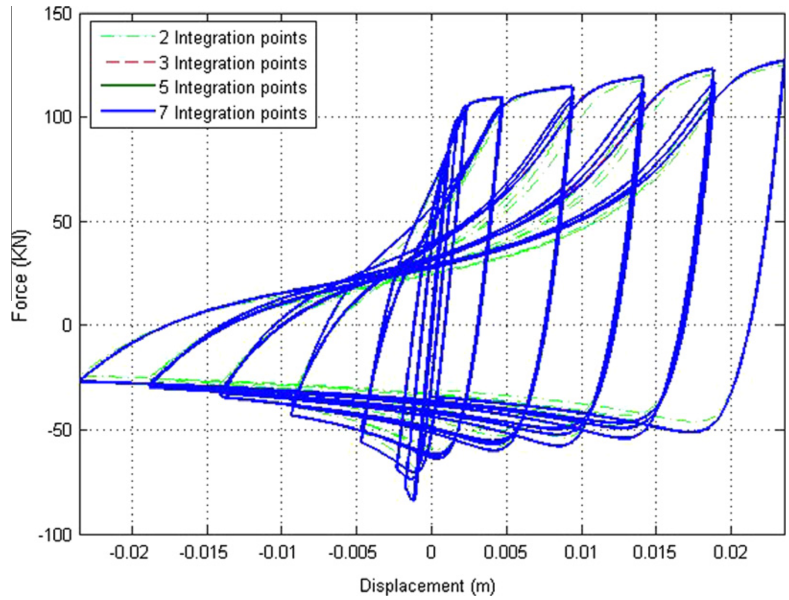

Fig. 8. Effect of changing the number of integration points for the brace in the numerical model to the force displacement response using eight non-linear beam–column elements per brace over the unstiffened length.

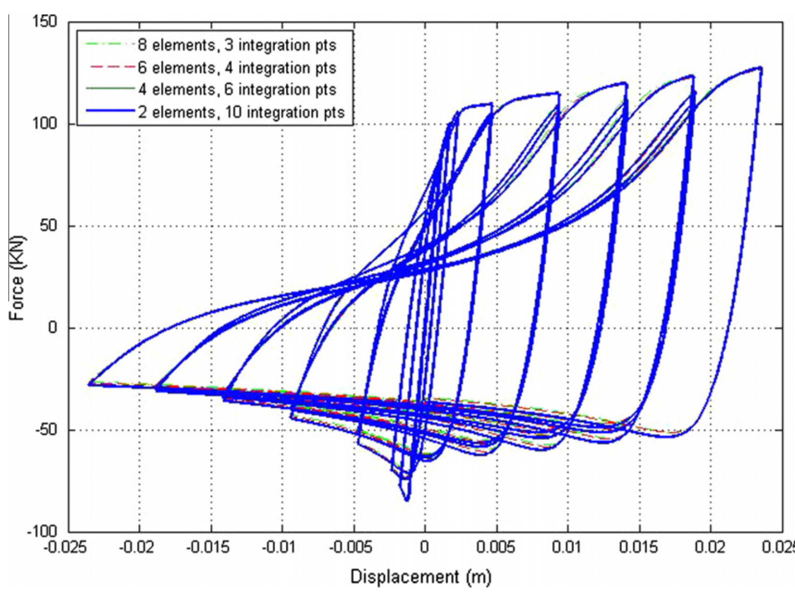

Fig. 9. Effect of changing the number of elements and integration points for the unstiffened brace in the numerical model to the force displacement response using different non-linear beam–column element per brace and different integration points per element.

study, a minimum number of ten integration points is recommended while using two elements per brace.

To assure the validity of the numerical model, a comparison between the performance of the model to cyclic and monotonic loading is carried out in OpenSees for the same brace element as shown in Fig. 11. Acceptable results are found, specifically for the first and post buckling loads. However, maximum tensile forces in the brace member during the first cycle at each new displacement demand were higher than those predicted in monotonic tests in post yield range. An explanation for this difference may be the numerical rounding, especially with the massive number of numerical operations required. On the other hand, the maximum tensile force experienced in second and third cycles at a given displacement amplitude were reduced due to Baushinger effect.

4. Low cyclic fatigue modelling

Brace steel members subjected to cyclic loading suffer stages of buckling and yielding. After the occurrence of buckling, rotational plastic hinges will form. They experience large rotational demands undergoing large strain deformation histories causing fracture due to low cyclic fatigue. Fatigue process consists of three stages: initial crack nucleation, progressive crack growth across the part and finally a sudden fracture of the remaining cross section. The fatigue strength of a material is determined experimentally. This is achieved by subjecting test specimens to repeated loads or strains of specified amplitude or ranges, and determining the number of cycles required to produce failure [29]. ASTM [30] defines fatigue life, N_f, as the number of cycles of stress or strain of a specified

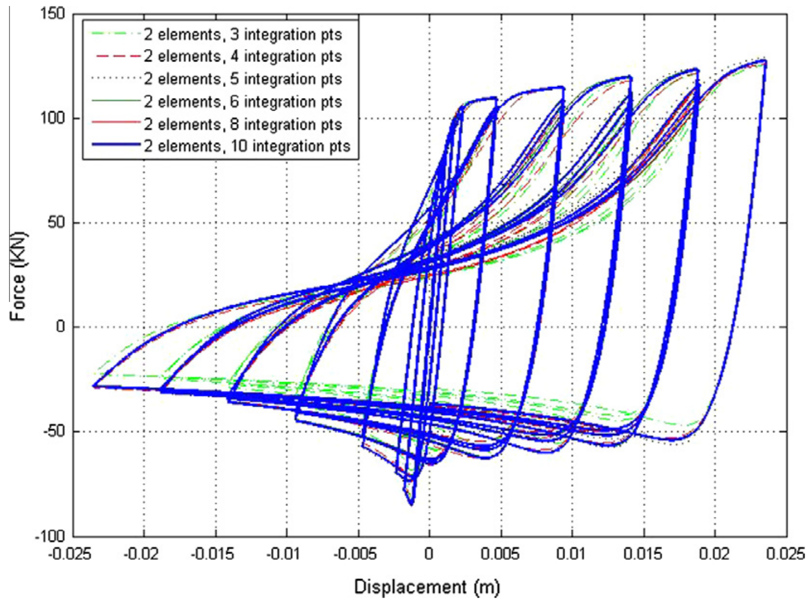

Fig. 10. Effect of changing the number of integration points for the brace in the numerical model to the force displacement response using two non-linear beam–column elements per brace over the unstiffened length.

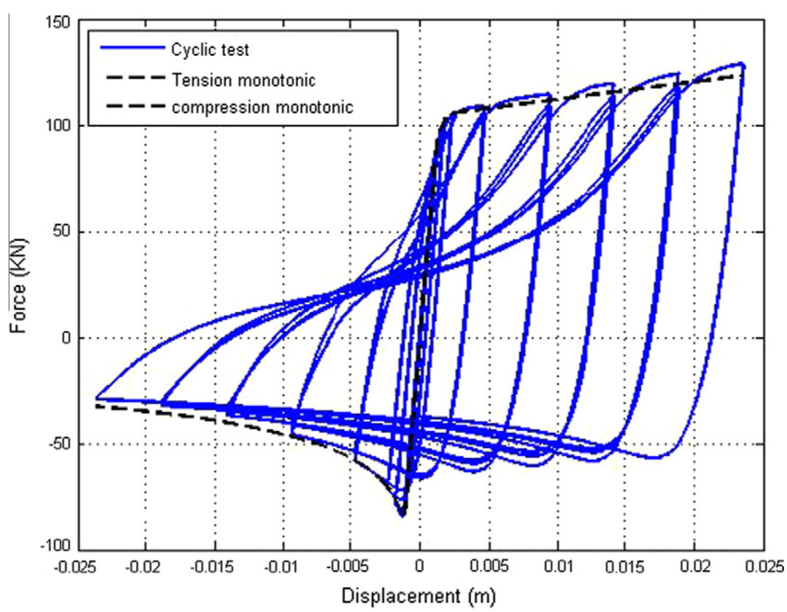

Fig. 11. Comparison of response of numerical model to monotonic and cyclic loading.

character that a given specimen sustains before failure of a specified nature occurs.

Occurrence of local buckling within the plastic hinge, increases strain demands causing faster fracture initiation. When local buckling occurs, and the braces deform in compression, cracks will form after the braces are loaded in tension [9,31–33]. From the cyclic tests carried out by Goggins [20] and discussed earlier, it is found that slender braces can exhibit better fracture life performance than braces with low member slenderness ratio. A possible reason of that is the occurrence of local buckling within the plastic hinge for stockier members, which increases strain demands and reduce fatigue life.

To quantify the damage in braces, a discrete form of damage accumulation rule called Palmgren–Miner's rule can be used. This rule describes the damage in the low cycle fatigue with constant plastic strain amplitude and associated with the relative reduction of deformability to quantify the damage for cyclic loading, DI, as [34]

$$DI = \frac{4n\Delta\varepsilon_p}{4N_f\Delta\varepsilon_p} \tag{1}$$

where $\Delta\varepsilon_p$ is the plastic strain amplitude, n is the current number of cycles and N_f is the number of life cycles. In Eq. (1), the numerator $4n\Delta\varepsilon_p$ denotes the current plastic strain and the denominator $4N\Delta\varepsilon_p$ denotes the total plastic deformability, which varies depending on the given plastic strain amplitude. However, during earthquakes the amplitude of the cycles is not constant. As such, the amplitude of each cyclic excursion in deformation history and the number of cycles at each amplitude identified can be computed using a rainflow cycle counting method [25,35,36]. Damage for each amplitude of cycling is estimated by

$$DI_i = \frac{n_i}{N_{fi}} \tag{2}$$

where n_i is the number of cycles at an amplitude and N_{fi} is the number of constant amplitude cycles of that amplitude necessary to cause failure. Manson [37] and Coffin [38] working independently in fatigue problems, proposed a characterization of fatigue life based on the plastic strain amplitude. They noted that when the logarithm of the plastic strain amplitude experienced in each cycle, ε_i, was plotted against the logarithm of the number of cycles to failure, N_f, a linear relationship resulted for metallic materials as shown in the following equation [39]:

$$\varepsilon_i = \varepsilon_0 (N_f)^m \tag{3}$$

where ε_o is the fatigue ductility coefficient which is the material parameter that roughly indicates the strain amplitude at which one complete cycle on a virgin material will cause failure, and m is the fatigue ductility exponent which is the material parameter which describes the sensitivity of the log of the total strain amplitude to the log of the number of cycles to failure.

Overall damage due to low cycle fatigue is estimated by linearly summing the damage for all of the amplitudes of deformation cycles considered (ε_i) [25]. During cycling, to get N_{fi} for current amplitude, constant coefficients ε_o and m for Eq. (3) should be known and Eq. (2) can be written as

$$DI_i = \frac{n_i}{10^{\left(\frac{\log\left(\frac{\varepsilon_i}{\varepsilon_0}\right)}{m}\right)}} \tag{4}$$

Uriz [25] developed and calibrated a low cycle fatigue model to be used with the Opensees fibre-based nonlinear beam-column model for simulating the large displacement and the inelastic buckling behaviour of steel struts. As described in OpenSees command language manual [24], in order to account for the effects of low cycle fatigue, a modified rainflow cycle counter has been implemented to track strain amplitudes. Rainflow cycle counting necessitate examination of the entire time strain history for each fibre at each time step, since the strain history changes as each increment of strain occurs where rainflow cycle counting analyses strain histories after the termination of loading to determine the number and the amplitude of the imposed cycles. Because of the computational effort involved in this procedure, a modified method is proposed by Uriz [25] that utilizes the traditional rainflow cycle counting method to accumulate damage, but does so by analyzing only a relatively short moving window of recent strain history. This cycle counter is used in Miner's Rule shown in Eq. (4) as the linear strain accumulation model based on Coffin-Manson log-log relationships describing low cycle fatigue failure. This material wraps around the parent material and does not influence the force–deformation relationship of the original material. Once the fatigue material model reaches a damage level of one, the resistance of the parent material becomes zero (1.0×10^{-8} is used to drop the stress of the material). If failure is triggered in compression, the material stress is dropped at the next zero-force crossing where compression force never drops to zero. The fatigue material assumes that each point is the last point of the history, and tracks damage with this assumption. If failure is not triggered, this pseudo-peak is discarded. The material also has the ability to trigger failure based on a maximum or minimum strain.

In summary, damage during each cycle is found based upon Palmgren–Miner's using coffin-Manson relationship where constant coefficient ε_o and m should be calibrated. Accumulated damage is found by using Palmgren–Miner's rule assuming the damage accumulated linearly using a modified rainflow cycle counting technique as in the following equation:

$$DI_{i+1} = DI_i + \frac{n_i}{10^{\left(\frac{\log\left(\frac{\varepsilon_i}{\varepsilon_0}\right)}{m}\right)}} \tag{5}$$

If in any point the damage Index (DI) become one or more, then the corresponding fibre in the cross section is removed from the cross section by reducing its stress and stiffness to zero.

Uriz [25] calibrated OpenSees low cyclic fatigue model for four different sections and found the constant coefficient for each of them as follows: wide flange sections (ε_o = 0.191, m = −0.458), hollow structural section (HSS) members (ε_o = 0.095, m = −0.5), buckling restrained brace (BRB) members (ε_o = 0.12, m = −0.458) and reinforcing bars (ε_o = 0.081, m = −0.43). From the last values it is evident that most of the material models have a very similar value for the parameter, m, but the value of ε_o varies significantly between section types. For the HSS, the fatigue parameters where calibrated for 6"X6"X3/8" HSS only. In this paper, new parameters representing different brace sections are proposed. It is important to know that the model doesn't account for the local buckling effect and the computed strains do not represent the actual strains in the member, but parameters used in the model can be calibrated to compensate for this fact.

To check a consistent model for the minimum number of elements that can be used for the brace using the fatigue model and the number of integration points per element, numerical models are tested using different number of elements and constant number of integration points. It is found that using six integration points per element with four elements or more gives consistent results as shown in Fig. 12. On the other hand, using 10 integration points per element with two elements for the numerical model is satisfactory and gives the same results as dividing the brace into more elements, as shown in Fig. 13.

The numerical models incorporating the fatigue model with the parameters suggested by Uriz [25] for hollow structural section (HSS) members (ε_o = 0.095, m = −0.5) did not represent the real behaviour of the physical specimens tested by Goggins [20] during the cyclic loading, where the numerical model force decreases faster than the real behaviour of the specimen. Neither did numerical models incorporating the fatigue parameters obtained by Nip et al. [40] from physical low cyclic fatigue tests on coupons taken from HSS members, which were on average found to be ε_o = 0.4027 and m = −0.6392 for cold formed carbon steel. On the other hand, Santagati et al. [41] calibrated the parameters m and ε_o for rectangular hollow section brace members by comparing the results of numerical simulations against the experimental behaviour of 32 HSS specimens found in literature. Based on this calibration they recommended a constant value of the slope m equal to −0.458 and a limit strain value ε_o equal to 0.07. Again, utilising these parameters in numerical models did not represent the real behaviour of the physical specimens tested by Goggins [20] during the cyclic loading. Thus, the model was calibrated using new parameters that can represent the behaviour of the specimens. After many trials, it is found that by calibrating the fatigue parameters in the numerical model to ε_o = 0.19 and m = −0.5, better results are achieved, at least for the sections tested by Goggins [20], as will be shown in the next section. Further, independent tests by Nip et al. [19] are used to validate this numerical model. It is found that using the fatigue parameters obtained by calibrating the model using the tests of Goggins [20] gave better predictions of the fracture life for most of the specimens, as will be shown in next section and Tables 1 and 2. Furthermore, this model was subsequently

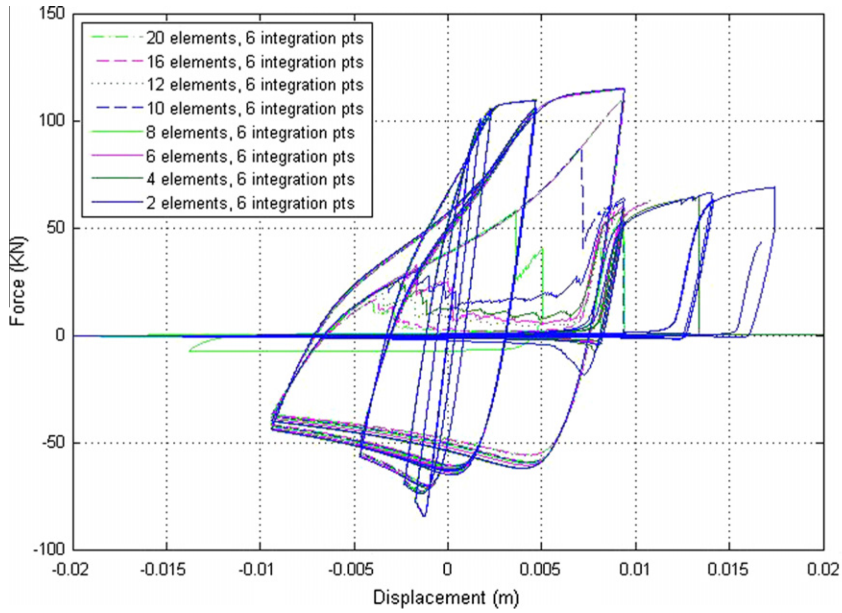

Fig. 12. Effect of changing the number of elements for the brace in the numerical model while using the fatigue model to the force displacement response using different number of non-linear beam–column element per brace and 6 integration points.

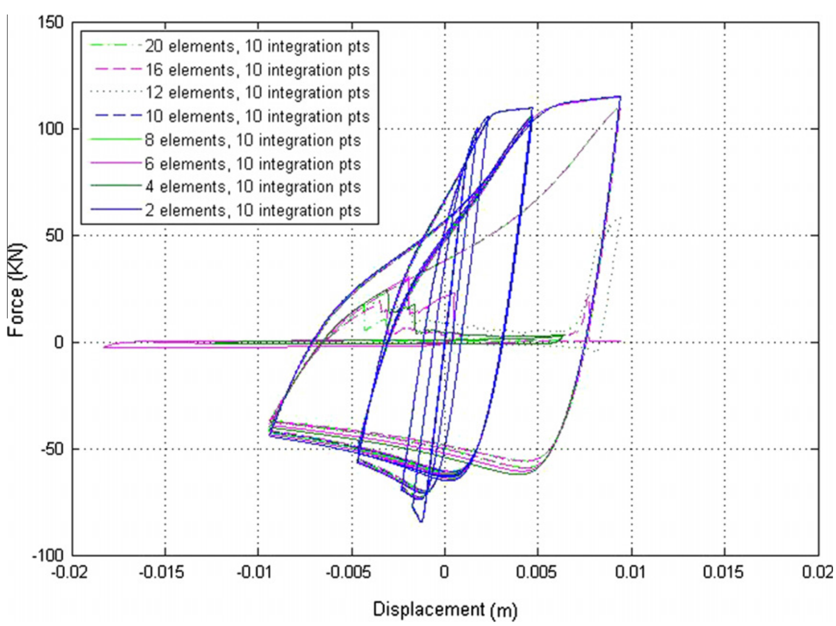

Fig. 13. Effect of changing the number of elements for the brace in the numerical model while using the fatigue model to the force displacement response using different number of non-linear beam–column element per brace and 10 integration points.

validated by comparing predictions from NLTHA to measured performance of brace members in full scale shake table tests [42].

5. Verification of the numerical model

OpenSees numerical models were studied for fifteen cyclic test specimens carried out by Goggins [20] and sixteen cyclic test specimens carried out by Nip et al. [19]. Cyclic tests were having different dimensions, lengths, normalised slenderness ratios, and material properties, as shown in Tables 1 and 2. Most of the parameters for the numerical models were taken the same as the ones found on the tests. Strain hardening in the numerical model was ignored in many cases. However, in some models it was necessary to include a low value of strain rate (<0.008) to improve stability of the analysis. Full fixity is assumed for end conditions. Yield strengths used in the numerical model for the cold form specimens carried out by Goggins [20] are taken as the increased average yield strength, f_{ya}, of the cross-section due to cold working as specified in Eurocode 3 [43] without using the upper limit value as the following equation:

$$f_{ya} = f_{yb} + \frac{knt^2}{A_g}(f_u - f_{yb}) \tag{6}$$

where f_{yb} is the basic yield value of sheet taken from coupon tests, A_g is the gross cross sectional area (mm^2), t is the design core thickness of the steel material before cold forming (mm), n is the number of 90° bends in the cross-section with an internal radius $r \leqslant 5t$ (fractions of 90° bends are counted as fractions of n), k is a numerical coefficient that depends on the type of forming (k = 7 for cold rolling and k = 5 for other methods of forming) and f_u is the basic ultimate tensile strength of sheet taken from coupon test. Goggins [20] found that Eq. (6) gives more accurate results when an upper limit is not apply. For the tests of Nip et al. [19] the yield strengths are taken as the offset yield strengths with a value set at 0.2% of the strain. This offset yield point is used normally for high strength steel which doesn't exhibit a yield point. It is known that the material properties of cold-formed sections vary around the cross-section due to the different levels of cold-work during forming. For example, Wilkinson and Hancock [44] found that the yield stress of the short opposite face of the welded face was on average 10% higher than that of the adjacent longer faces in the rectangular hollow sections (RHS). Moreover, they found that the yield stress obtained from the corner coupons was on average 10% higher than that of the opposite face. The corner yield strength is higher than the flat faces of the RHS, although the thickness is less than flat sections. In this study, average yield strength taking account of enhanced yield strength from cold forming has been used for the section and same thickness was assumed for the perimeter.

A comparison between the hysteretic axial force–axial displacement response for the tests and the numerical model is carried out and shown from Figs. 14–35. Tables 1 and 2 give section properties of the specimens, normalised slenderness about the Y–Y axis as defined in Eurocode 3 [21], $\lambda_{y\text{-}y}$, where the effective length is assumed to be 0.5L, yield strength, f_y, initial camber used in the numerical model, number of cycles needed to fracture for both physical tests and numerical model. Furthermore, ratios of the maximum tensile force (F_{max}), initial buckling load (F_c), the total energy dissipated by the specimens (W_{tot}) and the energy dissipated by the specimens at the first cycle of ductility of 4 ($W_{\mu=4}$) found from the numerical models and those measured from the physical tests are given in Tables 1 and 2.

5.1. Buckling and tensile loads

From Tables 1 and 2, it is found that there is a relatively good agreement between the numerical model and physical tests results of the maximum tensile forces (F_{max}) and initial buckling loads (F_c) for most of the specimens investigated. Moreover, the calibrated models had average ratios of numerical model to physical test model values for F_{max} and F_c of 0.93 and 0.95, respectively, with corresponding coefficients of variation (C_V) of 0.11 and 0.08, respectively (Table 1). The models were validated for cold-formed carbon steel, hot-rolled carbon steel, and cold-formed stainless steel by comparing predictions from the numerical model to findings from experimental physical tests carried out by Nip et al. [19], where average ratios of numerical model to physical test model values for F_{max} and F_c was 1.08 and 1.00, respectively, with corresponding C_V values of 0.09 and 0.09, respectively (Table 2). Thus, the equivalent mean values for F_{max} and F_c for the total 31 specimens studied were 1.01 and 0.98, respectively, with corresponding C_V values of 0.12 and 0.09, respectively.

Initial buckling loads obtained from the numerical model were found to be affected by initial camber provided at the middle of the specimens, which increases for slender braces with low initial buckling force. It is noticed that some post buckling cycles obtained from the numerical models are fatter and having more post buckling force than the cycles obtained from the physical tests. One possible explanation would be the limitation of the model that plane sections are assumed to remain plane, which will not capture the local buckling at the plastic hinge locations on the specimen. Local buckling phenomenon can be mitigated in practise by using low width to thickness ratio and Class 1 cross-section suggested in Eurocode 3 [21], which can form a plastic hinge with the rotation capacity required from plastic analysis without reduction in resistance that may be caused by local buckling.

While comparing the force–displacement response of the experimental and numerical model for 50×25×2.5×3300-CS-CF-G14 and 50×25×2.5×3300-CS-CF-G15, it is found that the yield capacity of the braces in the numerical model is lower than the yield capacity on the experiments (see Fig. 19). A possible explanation of that is the specific feature of the cold formed elements of increasing locally their yield strength due cold forming. Even though the average yield strength defined in Eurocode 3 [43] that takes into account the effect of cold forming is used, the yield displacement for experimental results is found to have higher values

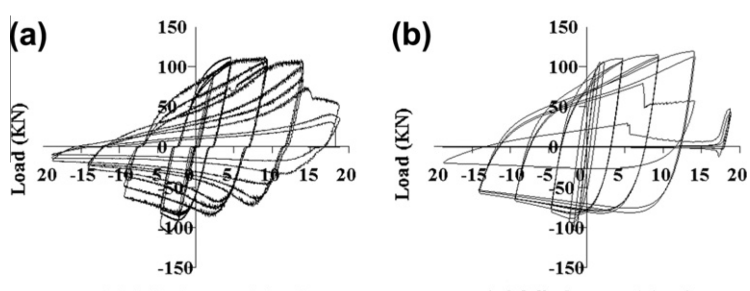

Fig. 14. (a) Physical test and (b) numerical model load displacement hysteretic loops for Specimen 40×40×2.5×1100-CS-CF-G2.

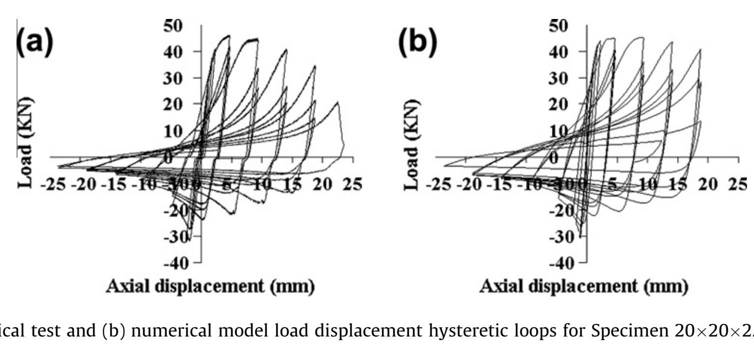

Fig. 15. (a) Physical test and (b) numerical model load displacement hysteretic loops for Specimen 20×20×2.0×1100-CS-CF-G4.

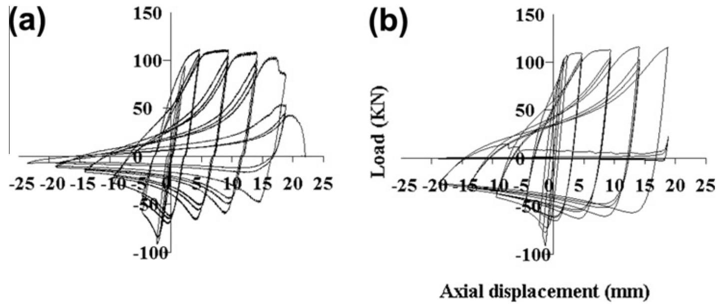

Fig. 16. (a) Physical test and (b) numerical model load displacement hysteretic loops for Specimen 50×25×2.5×1100-CS-CF-G6.

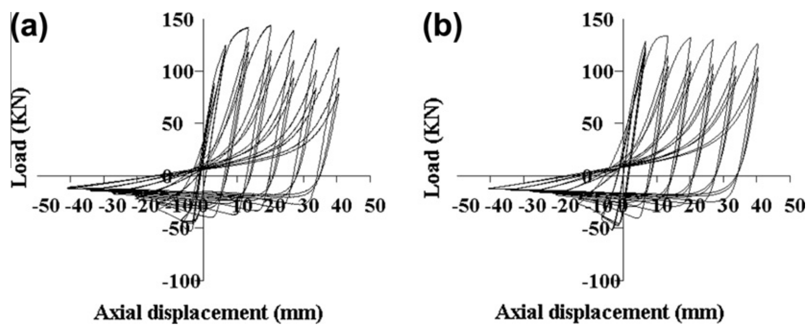

Fig. 17. (a) Physical test and (b) numerical model load displacement hysteretic loops for Specimen 40×40×2.5×3300-CS-CF-G8.

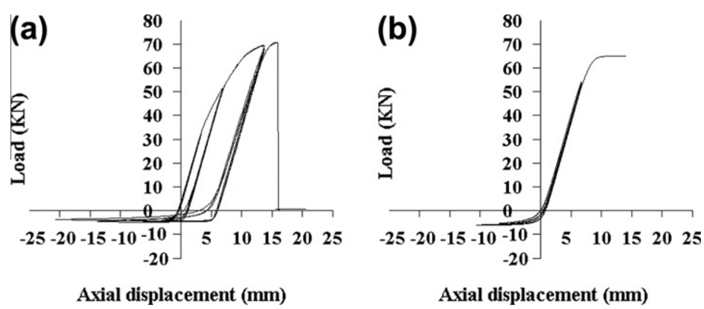

Fig. 18. (a) Physical test and (b) numerical model load displacement hysteretic loops for Specimen 20×20×2.0×3300-CS-CF-G10.

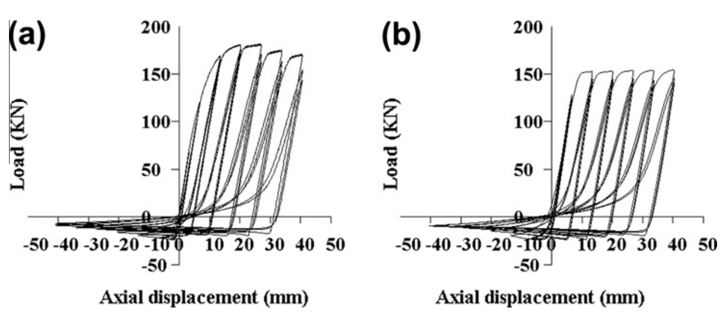

Fig. 19. (a) Physical test and (b) numerical model load displacement hysteretic loops for Specimen 50×25×2.5×3300-CS-CF-G14.

than the numerical model for these two tests, but was satisfactory for all other tests.

5.2. Fracture

For many tests, plastic hinges formed in the brace specimens after they experienced very large rotational demands and large strains, which caused fracture due to low cyclic fatigue. The numerical model incorporating a fatigue model could predict fracture after a number of cycles close to the ones obtained in the physical tests for the specimens tested until fracture occurred (see Tables 1 and 2). However, some of the physical test specimens suffered from early fracture at end connection, where the weld itself or the heat affected zone adjacent to the stiffener fractured during the physical tests, which is not accounted for in the numerical model. For this reason it is found that numerical model for

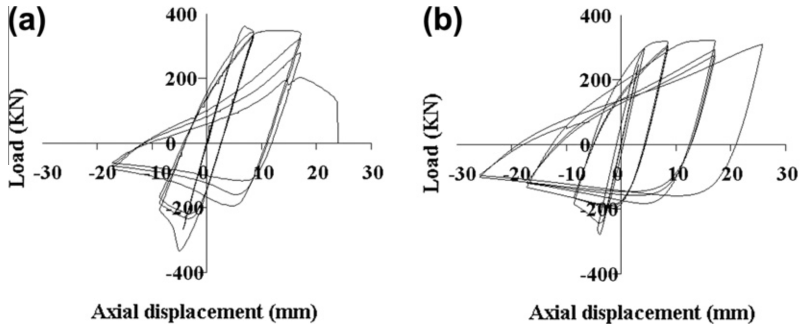

Fig. 20. (a) Physical test and (b) numerical model load displacement hysteretic loops for Specimen 60×60×3×2050-CS-HR-N16.

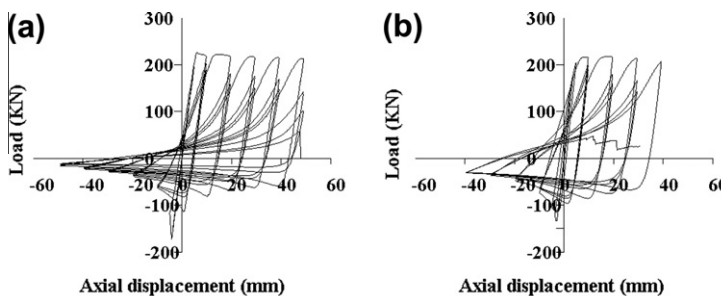

Fig. 21. (a) Physical test and (b) numerical model load displacement hysteretic loops for Specimen 40×40×3×2050-CS-HR-N17.

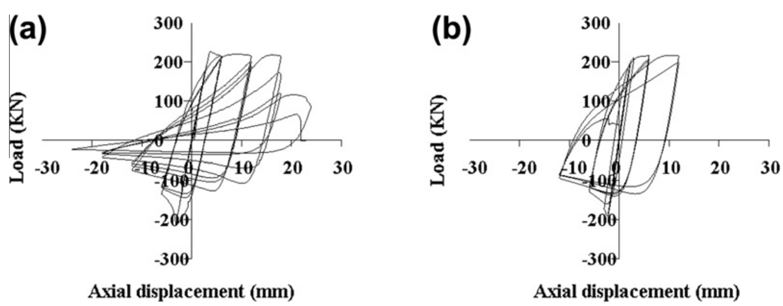

Fig. 22. (a) Physical test and (b) numerical model load displacement hysteretic loops for Specimen 40×40×3×1250-CS-HR-N18.

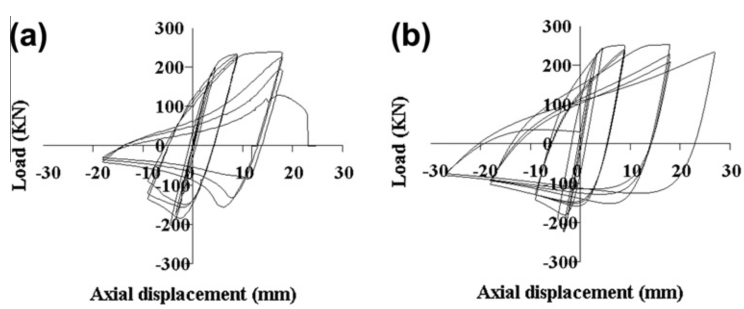

Fig. 23. (a) Physical test and (b) numerical model load displacement hysteretic loops for Specimen 60×60×3×2050-CS-CF-N19.

40×40×4.0×2050-CS-CF-N20, 40×40×3.0×2050-CS-CF-N21 and 60×40×3.0×2850-SS-CF-N25 had more cycles before capturing fracture as it is developed to have the fracture at the middle of the brace element not at the end connections. Specimens 40×40X2.5×3300-CS-CF-G7, 40×40×2.5×3300-CS-CF-G8, 40×40X2.5×3300-CS-CF-G9, 50×25×2.5×3300-CS-CF-G13, 50×25×2.5×3300-CS-CF-G14 and 50×25×2.5×3300-CS-CF-G15 were not tested to failure, and all of them survived displacement ductility demands between 5.6 and 9.5.

Tremblay [9] proposed a simple approach to find the total ductility reached at fracture, μ_f. This approach is related only to the normalised slenderness parameter, $\bar{\lambda}$, as follows:

$$\mu_f = 2.4 + 8.3\bar{\lambda} \tag{7}$$

where μ_f is the sum of the peak ductility reached in tension and the peak ductility attained in compression in any cycle before the half-cycle in tension in which failure of the brace is observed.

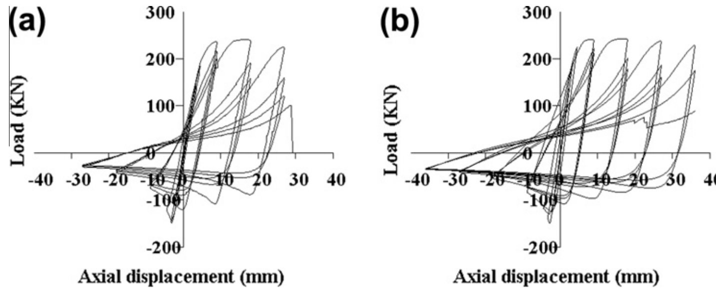

Fig. 24. (a) Physical test and (b) numerical model load displacement hysteretic loops for Specimen 40×40×4×2050-CS-CF-N20.

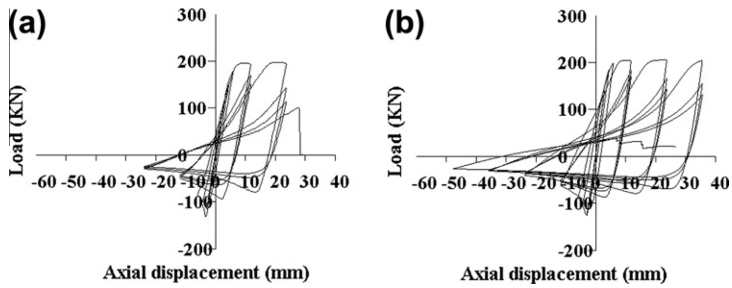

Fig. 25. (a) Physical test and (b) numerical model load displacement hysteretic loops for Specimen 40×40×3×2050-CS-CF-N21. Specimen failed at end connection.

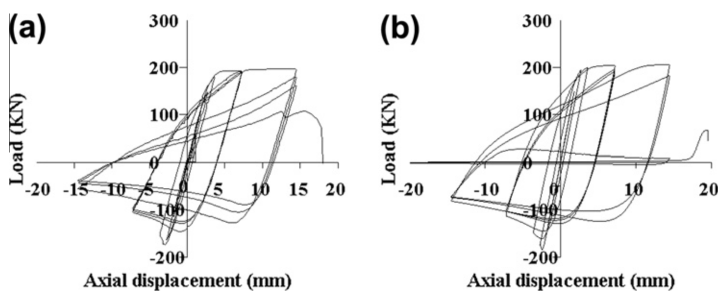

Fig. 26. (a) Physical test and (b) numerical model load displacement hysteretic loops for Specimen 40×40×3×1250-CS-CF-N22.

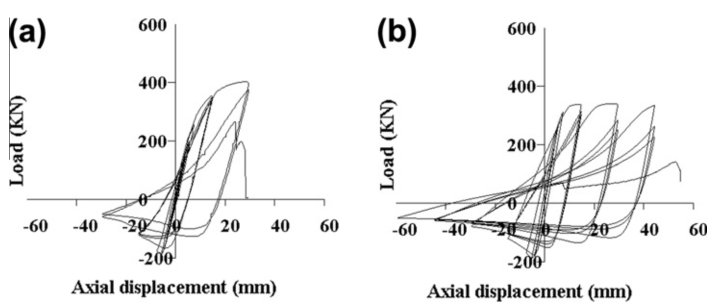

Fig. 27. (a) Physical test and (b) numerical model load displacement hysteretic loops for Specimen 60×60×3×2850-SS-CF-N23.

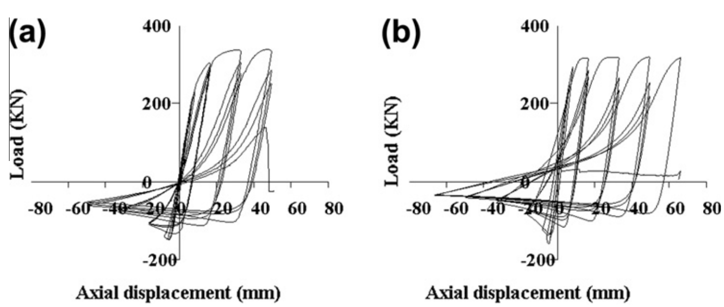

Fig. 28. (a) Physical test and (b) numerical model load displacement hysteretic loops for Specimen 50×50×3×2850-SS-CF-N24.

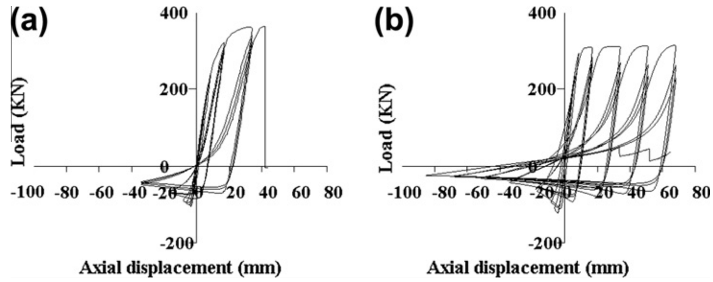

Fig. 29. (a) Physical test and (b) numerical model load displacement hysteretic loops for Specimen 60×40×3×2850-SS-CF-N25. Specimen failed at end connection.

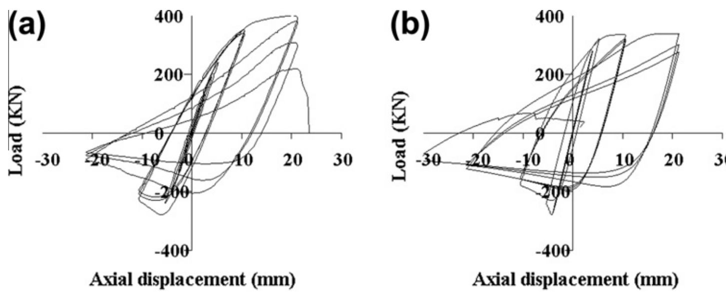

Fig. 30. (a) Physical test and (b) numerical model load displacement hysteretic loops for Specimen 60×60×3×2050-SS-CF-N26.

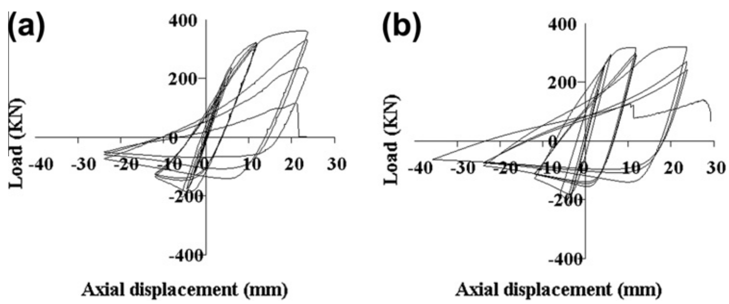

Fig. 31. (a) Physical test and (b) numerical model load displacement hysteretic loops for Specimen 50×50×3×2050-SS-CF-N27.

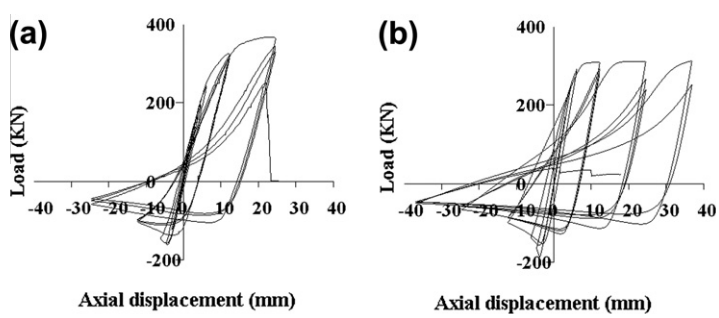

Fig. 32. (a) Physical test and (b) numerical model load displacement hysteretic loops for Specimen 60×40×3×2050-SS-CF-N28.

Moreover, Goggins et al. [17] used their physical test data to develop new relationships expressing the displacement ductility, μ_f, in terms of global slenderness, $\bar{\lambda}$, and width to thickness ratio (b/t) as shown in Eqs. (8) and (9).

$$\mu_f = -0.68 + 26.2\bar{\lambda} \quad (8)$$

$$\mu_f = 29.1 - 1.07(b/t) \quad (9)$$

However, Nip et al. [19] proposed new predictive expressions for the displacement ductility in terms of global slenderness ratio, $\bar{\lambda}$, and width to thickness ratio (b/t) for hot-rolled carbon steel, cold-formed carbon steel and cold-formed stainless steel as follows:

Hot-rolled carbon steel:

$$\mu_f = 3.69 + 6.97\bar{\lambda} - 0.05(b/t\varepsilon) - 0.19(\bar{\lambda})(b/t\varepsilon) \quad (10)$$

Cold-formed carbon steel:

$$\mu_f = 6.45 + 2.28\bar{\lambda} - 0.11(b/t\varepsilon) - 0.06(\bar{\lambda})(b/t\varepsilon) \quad (11)$$

Cold-formed stainless steel:

$$\mu_f = -3.42 + 19.86(\bar{\lambda}) + 0.11(b/t\varepsilon) - 0.64(\bar{\lambda})(b/t\varepsilon) \quad (12)$$

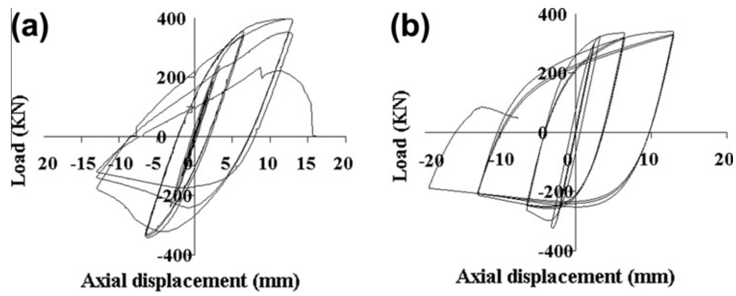

Fig. 33. (a) Physical test and (b) numerical model load displacement hysteretic loops for Specimen 60×60×3×1250-SS-CF-N29.

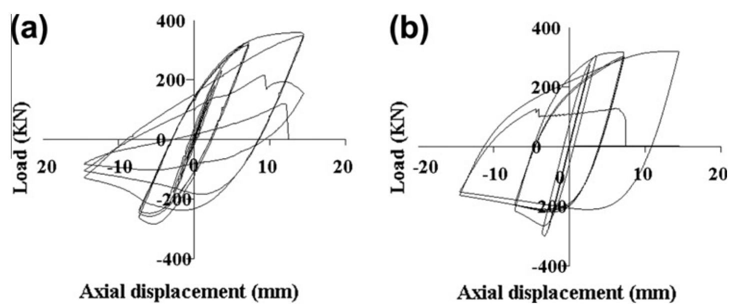

Fig. 34. (a) Physical test and (b) numerical model load displacement hysteretic loops for Specimen 50×50×3×1250-SS-CF-N30.

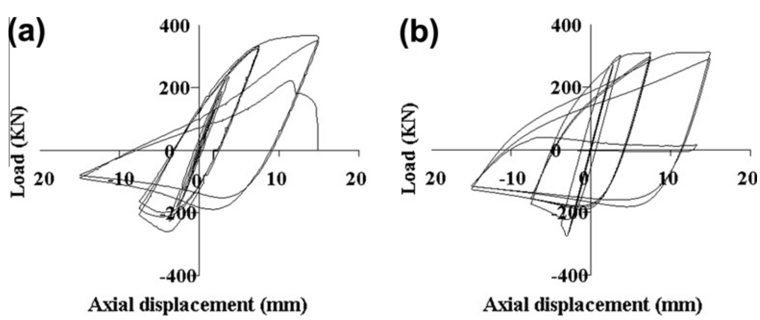

Fig. 35. (a) Physical test and (b) numerical model load displacement hysteretic loops for Specimen 60×40×3×1250-SS-CF-N31.

where $\bar{\lambda}$ is the normalised slenderness ratio, b is the width of the wider face of the section, t is the thickness of the section and $\varepsilon = \sqrt{235/f_y}$ where f_y is the yield strength.

Fig. 36 compares predicted displacement ductility values obtained from the numerical model to those obtained from the expressions established by Nip et al. [19]. It is found that Nip et al. [19] expressions for predicting displacement ductility gives close results to the values obtained from the numerical model. However, these relationships overestimated the displacement ductility for very slender specimens with slenderness ratio more than three as shown in Fig. 36.

5.3. Energy dissipated

As shown in Tables 1 and 2, and Fig. 37, the numerical model gave good predictions of the total energy dissipated, W_{tot}, and energy dissipated at the first cycle of ductility of 4, $W_{\mu=4}$, when compared to the results obtained from the physical tests during cyclic loading. However, some cycles obtained from the numerical models were found to be fatter than the cycles obtained from the tests, specifically for stockier specimens as the numerical model could not capture the local buckling. This is the reason why the energy dissipated results predicted from numerical model was slightly more than the energy dissipated from physical tests. Total energy dissipation for specimens 40×40×4.0×2050-CS-CF-N20, 40×40×3.0×2050-CS-CF-N21 and 60×40×3.0×2850-SS-CF-N25, which suffered from early fracture at end connection was less than the

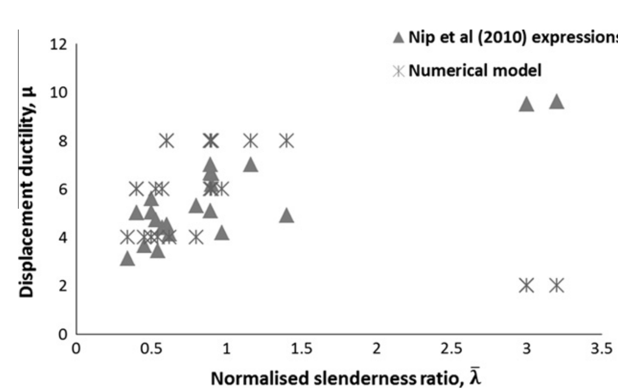

Fig. 36. Comparison of displacement ductility, μ, values obtained from the expressions established by Nip et al. [19] to the numerical model results.

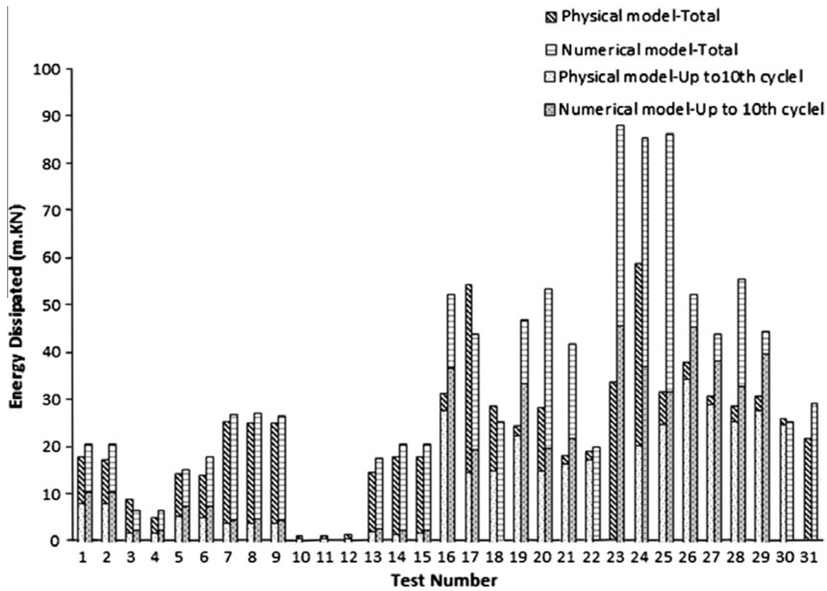

Fig. 37. Energy dissipated by specimens in physical tests [16,19] and the numerical models.

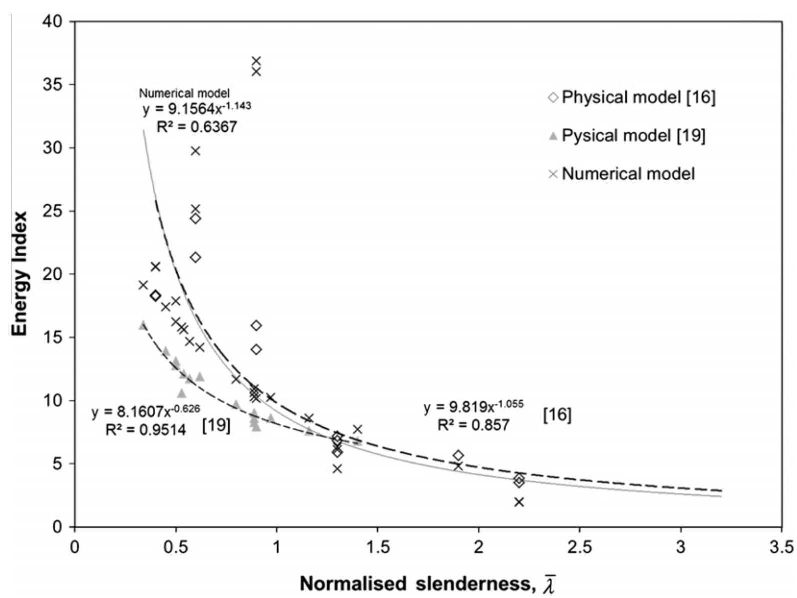

Fig. 38. Energy index versus slenderness for the first cycle at a ductility of four measured in physical tests [16,19] and obtained from numerical models.

energy dissipated obtained from the numerical model having more hysteretic cycles. However, for the specimens that survived 10 or more cycles, good correlation of energy dissipated were found when comparing the energy dissipated up to the 10th cycle (see Fig. 37).

Similar to the observations in the measured hysteretic loops of the physical test specimens, the stockier specimens dissipated more energy due to their larger cross-sectional areas and the significant yield plateaus they exhibited. Fig. 38 shows the energy index (the area under the load–axial deflection curve in both tension and compression regions during the first cycle at a ductility level of 4 normalised to the elastic energy of the strut) plotted against the normalised slenderness ratio. This shows how the energy dissipated is reduced with brace slenderness. As can be seen from Fig. 38, the numerical model gives good average prediction of the energy index of the first cycle at ductility of four for specimens over a large range of slenderness.

6. Summary and conclusion

In this paper, a study of the behaviour of braces, which are the main elements to dissipate energy in concentrically braced frames, is carried out. A numerical model is developed and found to be capable to simulate the hysteretic behaviour of braces. Nonlinear beam column elements with distributed plasticity are used, where the cross section of the brace is divided into fibres along the perimeter and across the thickness. In this model, the brace is suggested to be divided into a minimum of two elements using ten integration points per element. An initial camber on the middle of the brace is used to account for the overall buckling and a value between 0.1% and 1% of the length of the brace is found to give the best results for the first buckling load. A low cyclic fatigue model with new parameters is proposed and used to wrap the fibre based nonlinear beam column model in order to capture fracture in the braces. It has been shown in this study that this model can accurately predict the maximum displacement ductility demand of the brace members when fracture occurs.

In general, good agreement was found between the main response parameters of the numerical and physical tests. For example, average ratios of the maximum measured values to those obtained from the numerical model for tensile forces (F_{max}) and initial buckling loads (F_c) for the physical tests carried out by Goggins [20] and Nip et al. [19], excluding tests which failed at end connection, were 1 and 0.98, respectively. The corresponding coefficients of variation (C_V) were 0.13 and 0.09, respectively. Moreover, the mean values of the ratio of the total energy dissipated (W_{tot}) and the energy dissipated at the first cycle of ductility of 4 ($W_{\mu} = 4$) for the numerical model and the physical tests carried out by Goggins [20] and Nip et al. [19], excluding tests which failed at end connection, were found to be 1.30 and 1.12, respectively. The corresponding coefficients of variation (C_V) were 0.32 and 0.18, respectively. There was a difference in the response between the numerical model and some tests in the post buckling range and the hysteretic loops were fatter. One possible reason is that the model does not account for local buckling which should be taken into account in future research. However, in general the models captured the salient response parameters observed in the physical tests.

Acknowledgements

The fellowship provided by the College of Engineering and Informatics at the National University of Ireland, Galway is gratefully acknowledged by the first author. Data provided from colleagues at Imperial College in London is also gratefully acknowledged.

References

[1] Kahn LF, Hanson RD. Inelastic cycles of axially loaded steel members. J Struct Div ASCE 1976;102(5):947–59.
[2] Popov EP, Zayas VA, Mahin SA. Cyclic inelastic buckling of thin tubular columns. J Struct Div ASCE 1979;105(ST11):2261–77.
[3] Black GR, Wenger BA, Popov EP. Inelastic buckling of steel struts under cyclic load reversals. UCB/EERC-8O/4O. Berkeley (CA): Earthquake Engineering Research Center; 1980.
[4] Jain AK, Goel SC, Hanson RD. Hysteretic cycles of axially loaded steel members. J Struct Div ASCE 1980;106(8):1777–95.
[5] Popov EP, Black RG. Steel struts under severe cyclic loadings. J Struct Div ASCE 1981;107(9):1857–81.
[6] Ballio G, Perotti F. Cyclic behavior of axially loaded members – numerical-simulation and experimental-verification. J Construct Steel Res 1987;7(1):3–41.
[7] Archambault MH. Etude du comportement séismique des contreventements ductiles en X avec profiles tubulaires en acier. EPM/GCS-1995-09. Montréal (Que): Department of Civil Engineering, école Polytechnique; 1995.
[8] Mamaghani IHP, Usami T, Mizuno E. Inelastic large deflection analysis of structural steel members under cyclic loading. Eng Struct 1996;18(9):659–68.
[9] Tremblay R. Inelastic seismic response of steel bracing members. J Construct Steel Res 2002;58(5–8):665–701.
[10] Zhao XL, Grzebieta RH, Lee C. Void Filled cold-formed RHS braces subjected to large deformation cyclic axial loading. J Struct Eng ASCE 2002;128(6):747–53.
[11] Elchalakani M, Zhao X-L, Grzebieta R. Tests of cold-formed circular tubular braces under cyclic axial loading. J Struct Eng 2003;129(4). 507-514.
[12] Shaback B, Brown T. Behaviour of square hollow structural steel braces with end connections under reversed cyclic axial loading. Canadian J Civ Eng 2003;30(4):745–53.
[13] Tremblay R, Archambault MH, Filiatrault A. Seismic response of concentrically braced steel frames made with rectangular hollow bracing members. J Struct Eng 2003;129:1626–36.
[14] Broderick BM, Goggins JM, Elghazouli AY. Cyclic performance of steel and composite bracing members. J Construct Steel Res 2005;61(4):493–514.
[15] Elghazouli AY, et al., Shake table testing of tubular steel bracing members. Proc Inst Civ Eng – Struct Build 2005; 158(4): 229–41.
[16] Goggins JM et al. Experimental cyclic response of cold-formed hollow steel bracing members. Eng Struct 2005;27(7):977–89.
[17] Goggins JM et al. Behaviour of tubular steel members under cyclic axial loading. J Construct Steel Res 2006;62(1–2):121–31.
[18] Broderick BM, Elghazouli AY, Goggins J. Earthquake testing and response analysis of concentrically-braced sub-frames. J Construct Steel Res 2008;64:997–1007.
[19] Nip KH, Gardner L, Elghazouli AY. Cyclic testing and numerical modelling of carbon steel and stainless steel tubular bracing members. Eng Struct 2010;32(2):424–41.
[20] Goggins J. Earthquake resistant hollow and filled steel braces. PhD thesis. Dublin: Trinity College, University of Dublin; 2004.
[21] CEN, Eurocode 3: Design of steel structures – Part 1–1: General rules and rules for buildings. 2005, EN 1993-1-1:2005/AC:2009.
[22] ECCS –Technical Committee 1. Structural Safety and Loadings – Technical Working Group 1.3. Seismic design recommended testing procedure for assessing the behaviour of structural steel elements under cyclic loads, 1986, 1st ed. Brussels; 1986.
[23] CEN, Eurocode 8, design of structures for earthquake resistance – Part 1: General rules, seismic actions and rules for buildings. 2004, EN 1998–1:2004/AC:2009.
[24] McKenna F, Fenves GL, Scott MH, Object oriented program, OpenSees; Open system for earthquake engineering simulation; 2000. <http://www.opensees.berkeley.edu>.
[25] Uriz P. Towards earthquake resistant design of concentrically braced steel buildings. Berkeley: Department of Civil and Environmental Engineering, University of California; 2005.
[26] Spacone E, Filippou FC, Taucer FF. Fiber beam-column model for nonlinear analysis of R/C frames. I: Formulation. Earthquake Eng Struct Dyn 1996;25(7):711–25.
[27] Filippou FC, Fenves GL. Methods of analysis for earthquake-resistant structures. Earthquake engineering: from engineering seismology to performance-based engineering. Boca Rotan (FL, United States); CRC Press; 2004 [chapter 6].
[28] Wijesundara KK. Design of concentrically braced steel frames with RHS shape braces. PhD thesis. Pavia: European Centre for Training and Research in Earthquake Engineering (EUCENTRE); 2009.
[29] Duggan TV, Byrne J. Fatigue as a design criterion. The Macmillan press Ltd.; 1977.
[30] ASTM, E 1049–85, Standard practices for cycle counting in fatigue analysis. ASTM International; 2005.
[31] Gugerli H. Inelastic cyclic behavior of steel members. Ann Arbor (MI): Department of Civil Engineering, University of Michigan; 1982.
[32] Lee S, Goel S. Seismic behavior of hollow and concrete-filled square tubular bracing members. UMCE 87-11. Ann Arbor (MI): Department of Civil Engineering, University of Michigan; 1987.
[33] Shermann D. Designing with structural tubing. Eng J AISC 1996:(3rd Quarter);101–9.
[34] Xue L. A unified expression for low cycle fatigue and extremely low cycle fatigue and its implication for monotonic loading. Int J Fatigue 2008;30(10–11):1691–8.
[35] ASTM, ASTM E-1049 – Standard practices for cycle counting in fatigue analysis. West Conshohocken (PA); 2003.
[36] Fisher J, Kulak G, Smith I, A fatigue primer for structural engineers. ATLSS Report No. 97-11. National Steel Bridge Alliance, AISC: Chicago (IL); 1997.
[37] Manson SS. Behaviour of materials under conditions of thermal stress. In: Heat Transfer Symposium. University of Michigan Engineering Research Institute; 1953, p. 9–75.
[38] Coffin L. A study of the effect of cyclic thermal stresses on a ductile metal. Trans ASME 1954;1954(76). 931–50.
[39] Stephens RI et al. Metal fatigue in engineering. John Wiley & Sons, Inc.; 2001.
[40] Nip KH et al. Extremely low cycle fatigue tests on structural carbon steel and stainless steel. J Const Steel Res 2010;66(1):96–110.
[41] Santagati S, Bolognini D, Nascimbene R. Strain life analysis at low-cycle fatigue on concentrically braced steel structures with RHS shape braces. J Earthquake Eng 2012;16(Suppl. 1):107–37.
[42] Goggins J, Salawdeh S. Validation of non-linear time history analysis models for single storey concentrically braced frames using full scale shake table tests. Earthquake Eng Struct Dyn, in press.
[43] CEN, Eurocode 3 – Design of steel structures – Part 1–3: General rules – Supplementary rules for cold-formed members and sheeting; 2006, EN 1993-1-3:2006/AC:2009.
[44] Wilkinson, Hancock. Tests to examine compact web slenderness of cold-formed RHS. J Struct Eng 1998;124(10):1166–74.